Electronic Supplementary Material (ESI) for Journal of Materials Chemistry C.

Supporting Information

Concentration Palette Enabling Temperature-Responsive Luminescence Co-Modulations of Inorganic Phosphors for Thermally-Triggered Security Tag

*Yiyi Ou, Yunlin Yang, Fengkai Ma, Zeming Qi, Mikhail G. Brik, and Hongbin Liang**

Corresponding Author

Hongbin Liang

Email: cesbin@mail.sysu.edu.cn

Table of Contents

Materials and synthesis

Strontium carbonate ($SrCO_3$, 99.99%), boric acid (H_3BO_3, 99.99%), cerium oxide (CeO_2, 99.99 %), europium oxide (Eu_2O_3, 99.99 %), terbium oxide (Tb_4O_7, 99.99%) and sodium carbonate (Na_2CO_3, 99.99%) were purchased from Aladdin company (https://www.aladdin-e.com/). The epoxy resin reagent was purchased from Taobao shop (https://www.taobao.com/). All chemicals were used as received without any further purification.

Series of Ce^{3+}/Eu^{2+}/Eu^{3+}/Tb^{3+} singly-doped $Sr_3B_2O_6$ samples $Sr_{3-2x}Ce_xNa_xB_2O_6$ (denoted as SBO:xCe^{3+}, x = 0.01, 0.02), $Sr_{3-y}Eu_yB_2O_6$, (SBO:yEu^{2+}, y = 0.01, 0.02, 0.03), $Sr_{2.98}Eu_{0.01}Na_{0.01}B_2O_6$ (SBO:0.01Eu^{3+}), $Sr_{2.90}Tb_{0.05}Na_{0.05}B_2O_6$ (SBO:0.05Tb^{3+}) and Ce^{3+}, Eu^{2+} co-doped samples $Sr_{2.96-z}Ce_{0.02}Na_{0.02}Eu_zB_2O_6$, (SBO:0.02$Ce^{3+}$, z$Eu^{2+}$; z = 0.01, 0.02, 0.03) were prepared via a high-temperature solid-state reaction method. Stoichiometric amounts of raw materials including $SrCO_3$, H_3BO_3, Na_2CO_3 (Na^+ acting as a charge compensator) and corresponding lanthanide oxides (CeO_2, Eu_2O_3, and Tb_4O_7) were weighed and thoroughly ground in the agate mortar. The obtained homogeneous mixture was transferred into corundum crucible and calcined at 1423 K for 6 h under H_2-N_2 (5%-95%) reducing ambience (for Ce^{3+}, Eu^{2+} and Tb^{3+} doped samples) or air atmosphere (for Eu^{3+} doped sample). After cooling down to room temperature (RT) in the furnace, the products were reground into powder for further characterizations.

Characterizations

The crystal structure and phase purity of samples were investigated with a RIGAKU D-MAX 2200 VPC X-ray diffractometer with Cu *Kα* radiation (λ = 1.5418 Å) at 40 kV and 26 mA. High quality XRD data for Rietveld refinement was collected over a scanning range of 10°-110° with an interval of 0.02° on a Bruker D8 Advanced X-ray diffractometer with Cu *Kα* radiation (λ = 1.5418 Å) operating at 35 kV and 35 mA. Rietveld refinement was performed with *TOPAS* Academic V4.1 software.[1] The high-resolution transmission electron microscopy (HR-TEM) image of sample was recorded with a FEI Tecnai G2 F30 transmission electron microscope at an accelerating voltage of 300 kV. For vibrational structure analysis of sample, the synchrotron-radiation far-infrared reflectivity spectrum was measured on the infrared spectroscopy and micro-spectroscopy beamline (BL01B) of National Synchrotron Radiation Laboratory (NSRL) in Hefei, China.[2] The related fitting procedure was performed with *RefFIT* software.[3] The Raman scattering spectrum was collected by a Renishaw inVia Qontor Raman microscope equipped with a laser excitation source at 532 nm. The photoluminescence excitation and emission spectra in UV-vis region as well as luminescence decay curves of lanthanide doped samples were collected on an Edinburgh FLS1000 spectrometer. A 450 W Xe900 xenon lamp was used as excitation source for steady-state luminescence measurement; a 340 nm EPLED pulsed light-emitting diode (Edinburgh Instruments) and a 450 nm EPL picosecond pulsed diode laser (Edinburgh Instruments) were used to measure the luminescence decay curves of Ce^{3+} and Eu^{2+}. The temperature-dependent luminescence measurements in 78-500 K were performed with an Oxford Optistat-DN cryostat, the sample temperature was controlled by a MercuryiTC temperature controller. The excitation spectrum in VUV-UV range was collected on the 4B8 beamline of Beijing Synchrotron Radiation Facility (BSRF), China.[4] Temperature-dependent emission spectra measurements on representative spots of colour-mode security tag were performed with an Ocean Optics QE65000 fibre optic spectrometer equipped with a cooled CCD sensor. Information identification on intensity-mode security tag were conducted by the OpenCV open source computer vision software library with a commercial USB camera carrying a 495 nm filter. Photos and videos of samples and security tags under daylight and UV light were taken with an Apple iPhone 8 Plus mobile phone.

Tag fabrications

The security tags were vertically constructed by transparent resin cover, steel mould filled with key phosphors, and steel substrate. Firstly, the designed mould with cut-outs was attached onto the substrate. Then the key phosphors were filled into the cut-outs to form the patterns. The resin cover was finally formed at the top by solidifying the mixture of epoxy resin and curing agent with a mass ratio of 2.5:1. The solidifying process was kept at 60 °C for 12 hours.

DFT calculations

The density functional theory (DFT) calculations were performed using Vienna Ab-initio Simulation Package (VASP) codes.[5,6] The $Sr_3B_2O_6$ compound was modelled by a unit cell containing 66 atoms. The Sr ($4s^24p^65s^2$), B ($2s^22p^1$) and O ($2s^22p^4$) were treated as valence electrons, and their interactions with cores were described by the projected augmented wave (PAW) method.[7] The atomic structure of SBO unit cell was optimized under the generalized gradient approximation (GGA) of the Perdew, Burke and Ernzerholf (PBE) exchange-correlation functional.[8] Table S10 listed the optimized atomic Cartesian positions. Then the optimized cell was used to calculate the band structure and density-of-states (DOS) results. Especially, for DOS calculation, the PBE0 hybrid functional with a fraction (32%) of Hartree-Fock (HF) exchange was applied to match the calculated band gap with the experimental result.[9] The convergence criteria for total energies and atomic forces were set to 10^{-6} eV and 0.01 eV·Å^{-1}, respectively. A cut-off energy of 650 eV for the plane wave basis was adopted. A 2×2×2 *k*-point grid in the Monkhorst-Pack scheme was used to sample the Brillouin zone during the band gap structure calculation while one *k*-point G was chosen for DOS calculation.

Fitting of far-IR reflectivity spectrum of SBO compound

The experimental far-IR reflectivity spectrum (Fig. 2d) was fitted with a Drude-Lorentz model with Lorentz oscillators for complex dielectric function parameterization:

$$\varepsilon(\omega) = \varepsilon_{\infty} + \sum_{k} \frac{S_k \omega_{p,k}^{2}}{\omega_{0,k}^{2} - \omega^{2} - k\gamma_k \omega} \tag{S1}$$

where ε_{∞} is the high frequency contribution to dielectric function, $\omega_{0,k}$, $\omega_{p,k}$, γ_k and S_k are the transverse frequency (eigen-frequency), "plasma" frequency, linewidth (scattering rate), and oscillator strength of k-th Lorentz oscillator, respectively. The normal-incidence reflectivity $R(\omega)$ was described with the above complex dielectric function $\varepsilon(\omega)$ as:

$$R(\omega) = \left| \frac{1 - \sqrt{\varepsilon}}{1 + \sqrt{\varepsilon}} \right|^2 \tag{S2}$$

Combining Equation (S1) and (S2), the experimental far-IR reflectivity spectrum was well fitted with the *RefFIT* program (Fig. 2d).[3] 28 Lorentz oscillators were adopted as compiled in Table S2. The IR-active vibrational modes below 400 cm^{-1} show relatively large oscillator strength values (> 0.1), indicating that the low-wavenumber vibrations mainly related to the [SrO_8] coordination make important contributions to far-IR vibrational spectrum.[10] The relatively weak Lorentz oscillators at ~ 973.4, ~ 1233, ~ 1259 and ~ 1287 cm^{-1}, for example, may be assigned as the symmetric stretching (ν_1, ~ 973.4 cm^{-1}) and asymmetric stretching (ν_3, ~ 1233, ~ 1259 and ~ 1287 cm^{-1}) of BO_3^{3-} internal vibrations, respectively.[10]

VRBE scheme construction of lanthanides in SBO compound

The VRBE scheme construction methods are provided in Refs. **11** and **12**. The following provides the detailed procedures of VRBE scheme construction for Ce^{3+} and Eu^{2+} in SBO case.

Firstly, the Coulomb repulsion energy $U(6, SBO)$ defined as the energy difference between the 4f ground state binding energies of Eu^{2+} and Eu^{3+} was evaluated to be ~ 6.84 eV via Equation (S3) with Ce^{3+} ε_c value (~ 1.55 eV) in SBO compound. Then the 4f ground state binding energy of Eu^{2+} $E_{4f}(Eu^{2+})$ was calculated to be ~ −3.99 eV with Equation (S4), and consequently $E_{4f}(Eu^{3+}) = E_{4f}(Eu^{2+}) - U(6, SBO) = -10.83$ eV.

$$U(6, SBO) = 5.44 + 2.834e^{-\varepsilon_c/2.2} \text{ (eV)} \quad \text{(S3)}$$

$$E_{4f}(Eu^{2+}) = -24.92 + \frac{18.05 - U(6, SBO)}{0.777 - 0.0353U(6, SBO)} \text{ (eV)} \quad \text{(S4)}$$

With the $O^{2-} \rightarrow Eu^{3+}$ charge transfer energy (~ 4.63 eV, Fig. S9), the host valence band top binding energy E_V was estimated as ~ −8.62 eV. The E_C of host conduction band bottom was also determined as ~ −1.06 eV by adding the host band gap of ~ 7.56 eV. The Eu^{2+} lowest 5d excited state binding energy E_{5d} (Eu^{2+}) was ~ −1.28 eV with its relaxed lowest excitation energy of ~ 2.72 eV.

For Ce^{3+} case, the 4f ground state binding energy $E_{4f}(Ce^{3+})$ was estimated as ~ −5.30 eV with the slightly-compound-dependent zigzag shapes of Ln^{2+} and Ln^{3+} 4f ground state binding energies for SBO case (Table S11). By adding the lowest 5d excitation energy of Ce^{3+} (~ 3.49 eV), the $E_{5d}(Ce^{3+})$ was evaluated as ~ −1.82 eV.

Energy transfer dynamics from Ce^{3+} and Eu^{2+}

For the energy transfer (ET) from Ce^{3+} to Eu^{2+} ions in SBO:2%Ce^{3+}, zEu^{2+} (z = 1%-3%), the Inokuti-Hirayama ET model that ignores the energy migration between diluted donor Ce^{3+} ions was adopted to analyze the donor Ce^{3+} decay properties.[13] The time-dependent emission intensity evolution of donor Ce^{3+} was then described below:

$$\frac{I(t)}{I(0)} = exp\left[-\left(\frac{t}{\tau_0}\right) - \frac{4\pi}{3} C_A \Gamma\left(1 - \frac{3}{S}\right) (C_{DA})^{3/S} t^{3/S} \right] \quad \text{(S5)}$$

where $I(t)$ and $I(0)$ represent the Ce^{3+} emission intensities at time t and initial time, respectively. τ_0 is the Ce^{3+} intrinsic lifetime (~ 38.2 ns, Fig. S3a), C_A is the acceptor concentration, $\Gamma(1-3/S)$ is the gamma function and S value indicates the multipolar interaction type between donor and acceptor [i. e. 6 for electric dipole-dipole interaction (EDD), 8 for electric dipole-quadrupole (EDQ) and 10 for electric quadrupole-quadrupole (EQQ)]. C_{DA} is the ET microparameter.

When we set $S = 6$, the best fitting quality of Ce^{3+} decay curves can be achieved (Fig. 4d), indicating the main mechanism of Ce^{3+}-Eu^{2+} ET process is electric dipole-dipole (EDD) interaction. Then the fitting parameters were also listed in Table S6. The average C_{DA} was obtained as ~ 1.422×10^{-46} m^6/s, and the critical distance (R_c) that corresponds to the balance between ET probability (P) from Ce^{3+} to Eu^{2+} and Ce^{3+} intrinsic decay rate ($1/\tau_0$) was calculated to be ~ 13.2 Å from the relation of $P = C_{DA}/R^S$, where $P = 1/\tau_0$ and $R = R_c$.

Supporting tables 1-11

Table S1. Refined structural parameters of SBO compound at RT. [a]

Atom	Wyck.	x	y	z	Occ.	B_{iso}(Å^2)
Sr1	18e	0.3559 (1)	0	0.2500	1	0.76 (8)
B1	12c	0	0	0.1169 (2)	1	1.39 (11)
O1	36f	0.1603 (3)	0.0104 (4)	0.1153 (2)	1	1.33 (17)

[a] R_{wp} = 8.92 %, R_p = 6.15 %, R_b = 7.75 %; Symmetry, trigonal; Space group, $R\bar{3}c$; $a = b$ = 9.046(1) Å, c = 12.57(1) Å; V = 890.8(1) Å^3; Z = 6.

Table S2. Fitting results of far-IR reflectivity spectrum of SBO compound. [b]

$\omega_{0,k}$	$\omega_{p,k}$	γ_k	S_k
95.10	43.57	6.491	0.21
128.3	99.07	18.63	0.60
139.3	53.66	10.29	0.15
178.0	74.33	13.13	0.17
184.5	74.79	12.27	0.16
192.8	82.34	14.46	0.18
203.1	93.90	17.98	0.21
215.0	111.8	21.64	0.27
228.5	110.4	21.75	0.23
246.9	187.1	22.34	0.57
277.7	93.00	13.88	0.11
308.8	87.54	13.64	0.080
318.7	98.94	21.35	0.096
333.4	115.6	32.64	0.12
352.8	91.08	37.05	0.067
497.2	156.6	160.8	0.099
586.8	103.4	78.66	0.031
604.3	62.35	4.924	0.011
615.6	33.86	3.564	0.0030
650.2	45.72	32.28	0.0050
676.8	52.32	27.26	0.0060
708.4	128.5	21.97	0.033
721.9	97.67	17.45	0.018
973.4	270.6	287.8	0.077
1193	259.3	26.49	0.047
1233	277.9	45.04	0.051
1259	332.8	43.86	0.070
1287	139.1	36.93	0.012

[b] $\varepsilon_\infty = 2.31$

Table S3. Temperature-dependent (100-500 K) CIE colour coordinates of SBO:2%Ce^{3+}, zEu^{2+} (z = 1%-3%).

Temperature (K)	CIE coordinates at different z values		
	1%	2%	3%
100	(0.49, 0.35)	(0.53, 0.37)	(0.56, 0.41)
200	(0.46, 0.36)	(0.50, 0.38)	(0.54, 0.43)
300	(0.37, 0.29)	(0.45, 0.36)	(0.51, 0.44)
400	(0.25, 0.16)	(0.36, 0.29)	(0.46, 0.41)
500	(0.19, 0.095)	(0.28, 0.20)	(0.39, 0.35)

Table S4. Related crystal-field-effect parameters of Ce^{3+} and Eu^{2+} in SBO.

Parameters	Ce^{3+}	Eu^{2+}
centroid shift (eV)	1.55	0.95
crystal field splitting (eV)	2.39	1.84

Table S5. Vibronic coupling parameters of Ce^{3+} and Eu^{2+} in SBO at 78 K.

Parameters	Ce^{3+}	Eu^{2+}
Stokes shift ($\times 10^3$ cm^{-1})	2.67	5.40
FWHM ($\times 10^3$ cm^{-1})	1.58	2.91
S	4.9	5.9
$\hbar\omega$ ($\times 10^3$ cm^{-1})	300	508
E_0 ($\times 10^3$ cm^{-1})	26.8	19.1

Table S6. Acceptor Eu^{2+} concentrations (C_A), fitted ET micro-parameters (C_{DA}), and determination coefficients (R_{adj}^2) of fitting procedures with Inokuti-Hirayama (I-H) model for donor Ce^{3+} luminescence decay curves at RT.

Eu^{2+} (at. %)	C_A (10^{25} m^{-3})	C_{DA} (10^{-46} m^6/s)	R_{adj}^2
0.01	6.742	2.352	0.9946
0.02	13.48	1.055	0.9915
0.03	20.23	0.858	0.9894
average	---	1.422	---

Table S7. Extracted temperature-dependent (78-500 K) Ce^{3+} emission lifetime values of SBO:2%Ce^{3+}, zEu^{2+} (z = 1%-3%).

Temperature (K)	Ce^{3+} lifetimes (ns) at different z values		
	1%	2%	3%
78	12.1	9.33	7.23
100	12.0	9.71	7.69
200	12.5	9.62	6.82
300	12.5	9.53	6.84
400	11.9	9.58	6.86
500	11.8	9.21	6.82

Table S8. Spectral-overlapping integrated area between Ce^{3+} emission (SBO:1%Ce^{3+}, λ_{ex} = 340 nm) and Eu^{2+} excitation spectra (SBO:1%Eu^{2+}, λ_{em} = 605 nm) at elevated temperature (100-500 K).

Temperature (K)	Spectral-overlapping integrated area
100	0.238
200	0.251
300	0.249
400	0.242
500	0.220

We selected the temperature-dependent spectra of Ce^{3+}/Eu^{2+} singly-doped samples (SBO:1%Ce^{3+} and SBO:1%Eu^{2+}) to investigate the influence of spectral thermal broadening on spectral overlapping between Ce^{3+} and Eu^{2+}. The results in Table S8 show that with the increase of temperature the spectral-overlapping integrated area between Ce^{3+} normalized emission (λ_{ex} = 340 nm) and Eu^{2+} normalized excitation (λ_{em} = 605 nm) spectra keeps stable among ~ 0.240 and does not present the evident thermal-driven enlargement. Consequently, the Ce^{3+}-Eu^{2+} ET process would not be obviously thermally accelerated. The Ce^{3+} emissions of co-doped samples could maintain the good thermal stability.

Table S9. Extracted temperature-dependent (78-500 K) Eu^{2+} emission lifetime (τ_t) and ratio (τ_t / $\tau_{78\,K}$) values of SBO:2%Ce^{3+}, zEu^{2+} (z = 1%-3%).

Temperature (K)	Eu^{2+} lifetimes (ns) at different z values		
	1%	2%	3%
78	1499	986.2	925.2
100	1471	937.5	968.4
200	1281	720.1	711.3
300	436.3	303.7	288.2
400	104.3	90.33	90.62
500	30.90	31.24	29.13
Temperature (K)	Eu^{2+} lifetime ratio at different z values		
78	1.00	1.00	1.00
100	0.98	0.95	1.05
200	0.85	0.73	0.77
300	0.29	0.31	0.31
400	0.07	0.09	0.10
500	0.02	0.03	0.03

Table S10. The optimized atomic Cartesian positions of SBO unit cell model via DFT calculation.

Atom	x	y	z	Atom	x	y	z
Sr	0.3526	0.0000	0.2500	O	0.0090	0.8512	0.8851
Sr	0.6474	0.0000	0.7500	O	0.8512	0.8421	0.1149
Sr	0.0000	0.3526	0.2500	O	0.1488	0.1579	0.8851
Sr	0.0000	0.6474	0.7500	O	0.0090	0.1579	0.3851
Sr	0.6474	0.6474	0.2500	O	0.9910	0.8421	0.6149
Sr	0.3526	0.3526	0.7500	O	0.1488	0.9910	0.3851
Sr	0.0192	0.3333	0.5833	O	0.8512	0.0090	0.6149
Sr	0.3141	0.3333	0.0833	O	0.8421	0.8512	0.3851
Sr	0.6667	0.6859	0.5833	O	0.1579	0.1488	0.6149
Sr	0.6667	0.9808	0.0833	O	0.8245	0.3424	0.4482
Sr	0.3141	0.9808	0.5833	O	0.5088	0.3243	0.2184
Sr	0.0192	0.6859	0.0833	O	0.6576	0.4822	0.4482
Sr	0.6859	0.6667	0.9167	O	0.6757	0.1845	0.2184
Sr	0.9808	0.6667	0.4167	O	0.5178	0.1755	0.4482
Sr	0.3333	0.0192	0.9167	O	0.8155	0.4912	0.2184
Sr	0.3333	0.3141	0.4167	O	0.6757	0.4912	0.7184
Sr	0.9808	0.3141	0.9167	O	0.6576	0.1755	0.9482
Sr	0.6859	0.0192	0.4167	O	0.8155	0.3243	0.7184
B	0.0000	0.0000	0.1161	O	0.5178	0.3424	0.9482
B	0.0000	0.0000	0.8839	O	0.5088	0.1845	0.7184
B	0.0000	0.0000	0.3839	O	0.8245	0.4822	0.9482
B	0.0000	0.0000	0.6161	O	0.4912	0.6757	0.7816
B	0.6667	0.3333	0.4494	O	0.1755	0.6576	0.5518
B	0.6667	0.3333	0.2173	O	0.3243	0.8155	0.7816
B	0.6667	0.3333	0.7173	O	0.3424	0.5178	0.5518
B	0.6667	0.3333	0.9494	O	0.1845	0.5088	0.7816
B	0.3333	0.6667	0.7827	O	0.4822	0.8245	0.5518
B	0.3333	0.6667	0.5506	O	0.3424	0.8245	0.0518
B	0.3333	0.6667	0.0506	O	0.3243	0.5088	0.2816
B	0.3333	0.6667	0.2827	O	0.4822	0.6576	0.0518
O	0.1579	0.0090	0.1149	O	0.1845	0.6757	0.2816
O	0.8421	0.9910	0.8851	O	0.1755	0.5178	0.0518
O	0.9910	0.1488	0.1149	O	0.4912	0.8155	0.2816

Table S11. Zigzag shapes of Ln^{2+}, Ln^{3+} 4f ground state binding energies relative to Eu^{2+}, Eu^{3+} cases in SBO compound.

Lanthanide	Ln^{2+} relative binding (eV)	Ln^{3+} relative binding (eV)
La	5.769	---
Ce	4.050	5.537
Pr	2.789	3.514
Nd	2.404	2.060
Pm	2.227	1.542
Sm	1.149	1.263
Eu	0	0
Gd	4.305	-1.310
Tb	2.925	3.428
Dy	2.093	1.764
Ho	2.192	0.6974
Er	2.328	0.6877
Tm	1.505	0.7722
Yb	0.2970	-0.2505
Lu	---	-1.797

The slightly-compound-dependent zigzag shapes of Ln^{2+}, Ln^{3+} 4f ground state binding energies in SBO compound were determined by the developed Jørgensen spin pairing theory,[12,14] in which the compound-independent tilt parameter [α (eV/pm)] and compound-dependent nephelauxetic ratio (β) were introduced to respectively consider the influence of lanthanide contraction and nephelauxetic effect. In this case, the $\alpha(2+)$ value is ~ 0.095 eV/pm, $\alpha(3+)$ is ~ 0.098 eV/pm and $\beta(2/3+)$ is 0.93.

Supporting figures 1-16

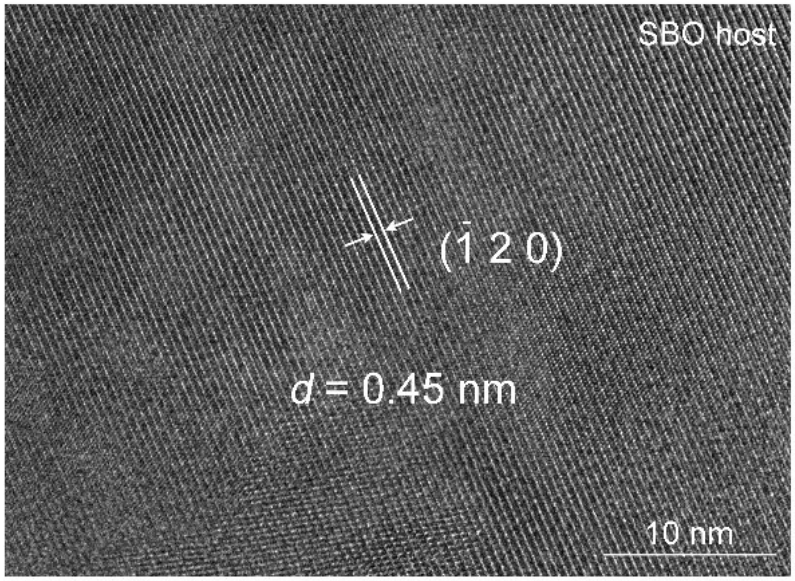

Fig. S1. High-resolution transmission electron microscopy (HR-TEM) image of SBO compound.

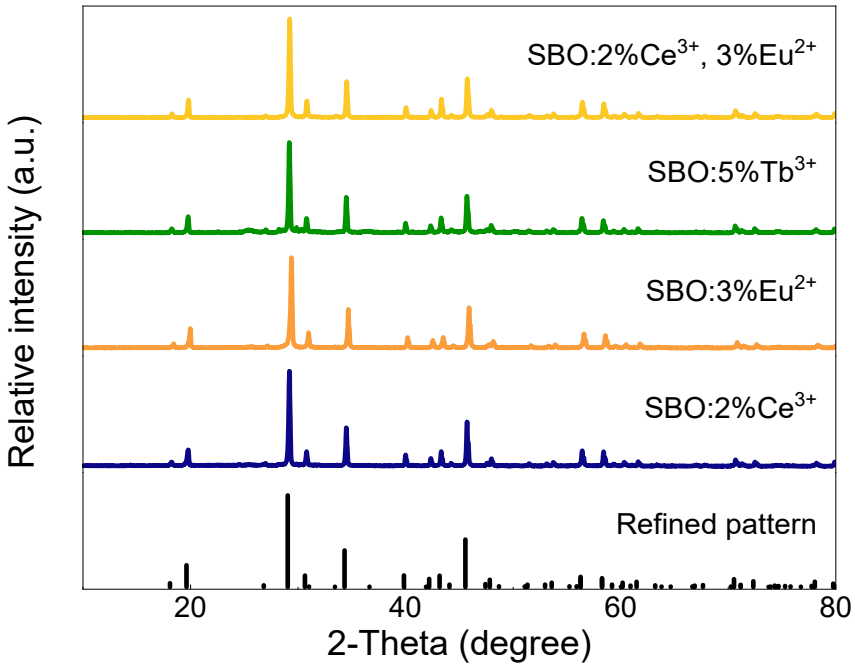

Fig. S2. Representative XRD patterns of lanthanide-doped SBO samples.

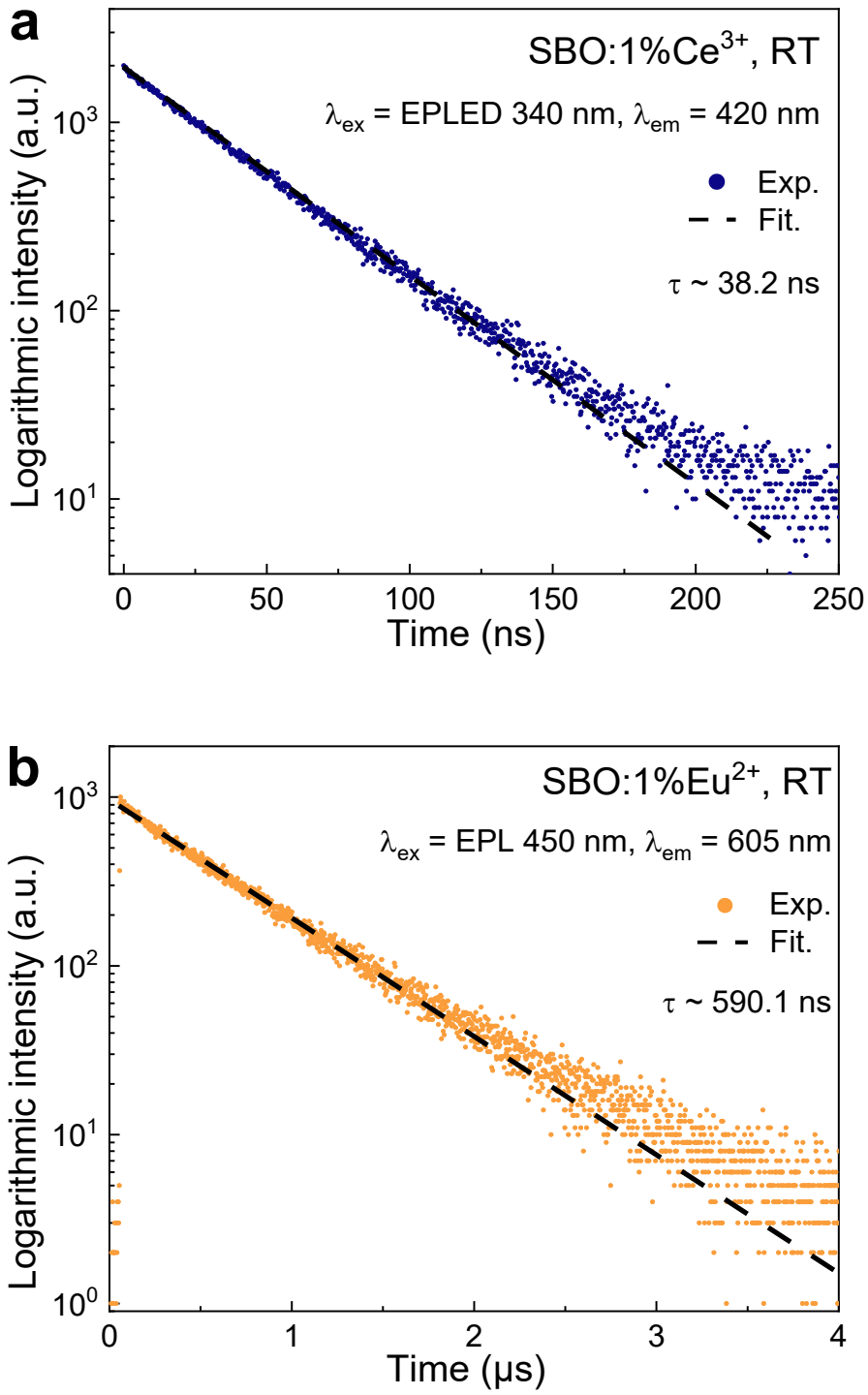

Fig. S3. (a) Luminescence decay curve (λ_{ex} = EPLED 340 nm, λ_{em} = 420 nm) of SBO:1%Ce^{3+} at RT. (b) Luminescence decay curve (λ_{ex} = EPL 450 nm, λ_{em} = 605 nm) of SBO:1%Eu^{2+} at RT.

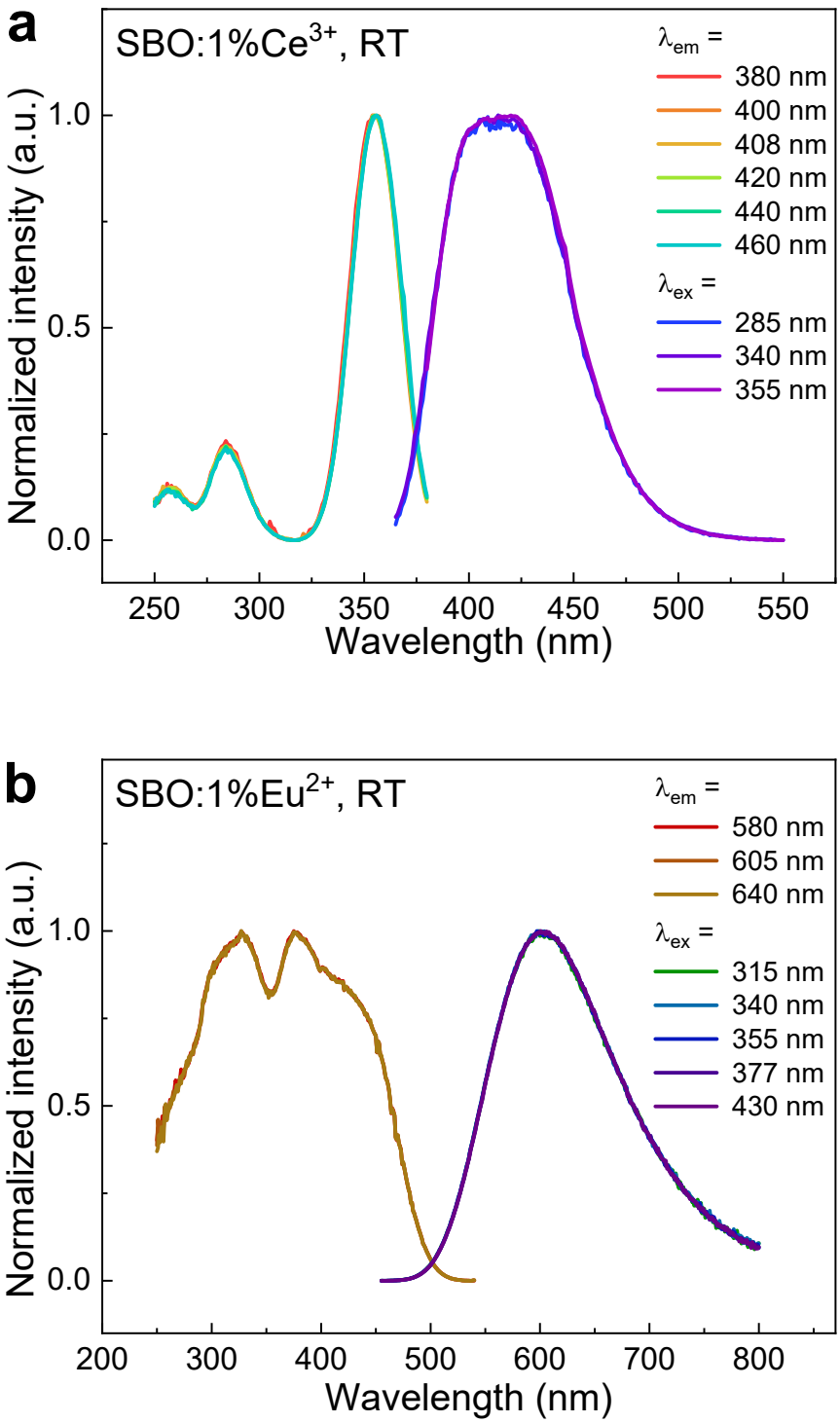

Fig. S4. (a) Highest-height normalized excitation (λ_{em} = 380, 400, 408, 420, 440, 460 nm) and emission (λ_{ex} = 285, 340, 355 nm) spectra of SBO:1%Ce^{3+} at RT. (b) Highest-height normalized excitation (λ_{em} = 580, 605, 640 nm) and emission (λ_{ex} = 315, 340, 355, 377, 430 nm) spectra of SBO:1%Eu^{2+} at RT.

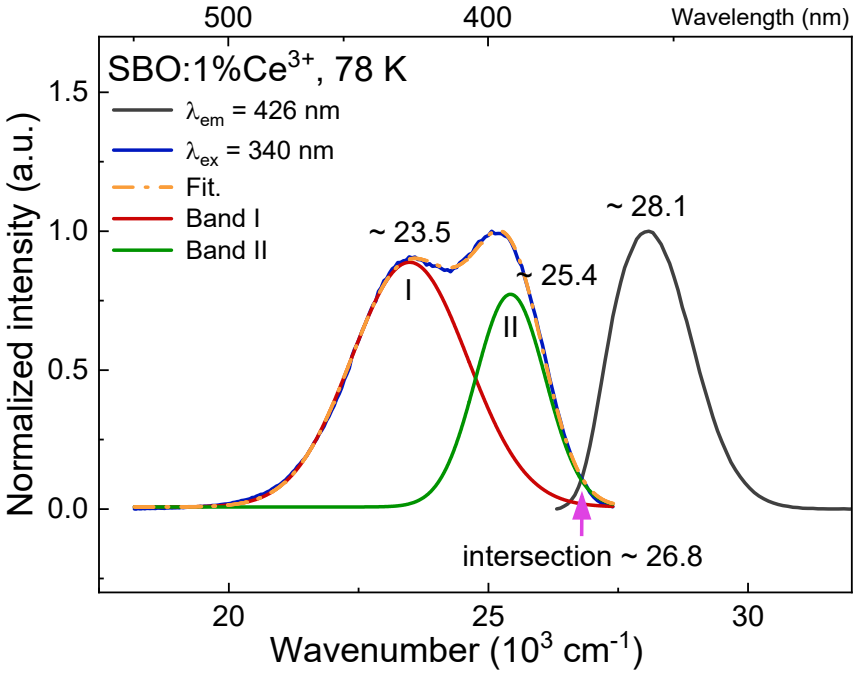

Fig. S5. Highest-height normalized excitation (λ_{em} = 426 nm) and emission spectra (λ_{ex} = 340 nm) of SBO:1%Ce^{3+} at 78 K. Two-components Gaussian fitting of emission profile are also presented.

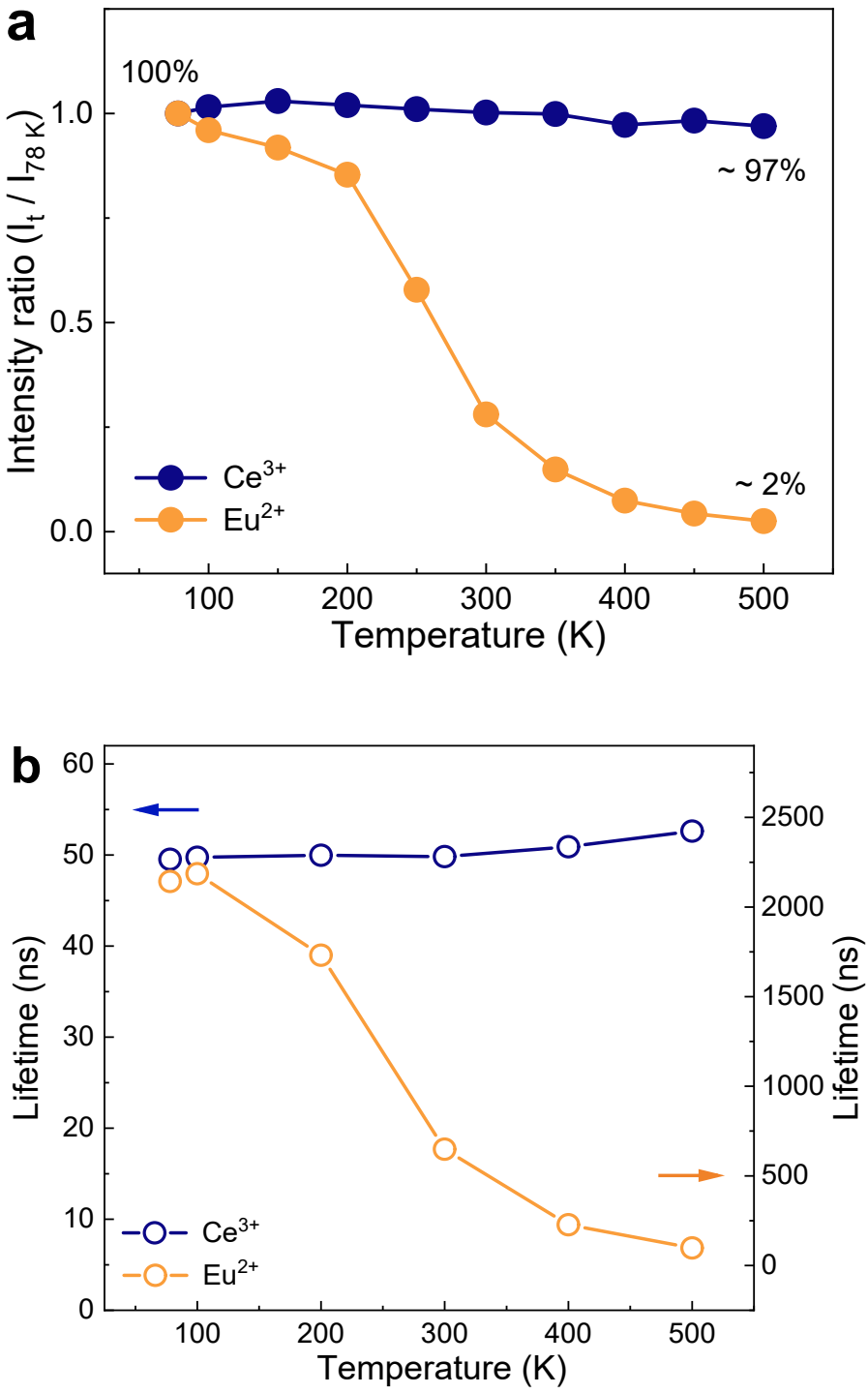

Fig. S6. Temperature-dependent (a) integrated emission intensity ratio (I_t / $I_{78\,K}$) and (b) extracted lifetime values of SBO:1%Ce^{3+} and SBO:1%Eu^{2+}, respectively.

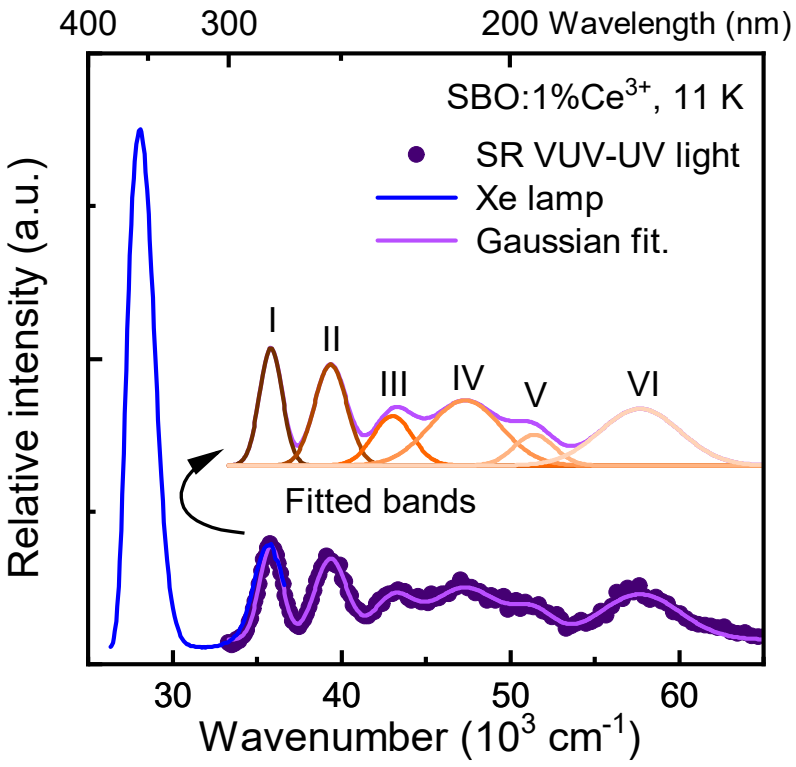

Fig. S7. VUV-UV excitation spectra of SBO:1%Ce^{3+} at 11 K and 78 K collected by using synchrotron-radiation (SR) VUV light source and laboratory xenon lamp, respectively, and corresponding Gaussian fitting.

To study the crystal field effect on Ce^{3+} 5d electrons, we apply the synchrotron-radiation (SR) vacuum ultraviolet (VUV) light source to collect the VUV-UV excitation spectrum (purple dot line) of SBO:1%Ce^{3+} at 11 K in Fig. S7. Compared with the result (blue line) recorded by laboratory xenon lamp at 78 K, they show good consistence in 33.0-37.0 × 10^3 cm^{-1} wavenumber range. The dominant band at ~ 28.1 × 10^3 cm^{-1} (~ 3.49 eV) in blue line pertains to Ce^{3+} $5d_1$ excitation band. Meanwhile, the purple dot line is well fitted with a sum of six Gaussian functions. The obtained band VI peaked at ~ 57.7 × 10^3 cm^{-1} is aligned to the SBO host exciton creation peak and provides an exciton creation energy (E^{ex}) of ~ 7.15 eV. Thus, the optical band gap (E_g) of SBO compound is estimated as ~ 7.56 eV by empirically adding an exciton binding energy [~ $0.008\times(E^{ex})^2$] to E^{ex},[15] which is consistent with the calculated value (~ 7.60 eV) in Fig. 2c. Referring to the five crystal-field-split 5d levels of Ce^{3+} in $Ca_3B_2O_6$ that is isostructural to SBO compound,[16] we attribute the other four fitted bands in Fig. S7 (band I, ~ 35.8 × 10^3 cm^{-1}; band II, ~ 39.4 × 10^3 cm^{-1}; band III, ~ 43.0 × 10^3 cm^{-1}; band IV, ~ 47.3 × 10^3 cm^{-1}) to Ce^{3+} $5d_i$ (i = 2, 3, 4, 5) excited states, respectively. As for band V peaked at ~ 51.4 × 10^3 cm^{-1}, it may be related to the absorption of defects near the host conduction band (CB) bottom. Some similar phenomena have been found in other systems.[17]

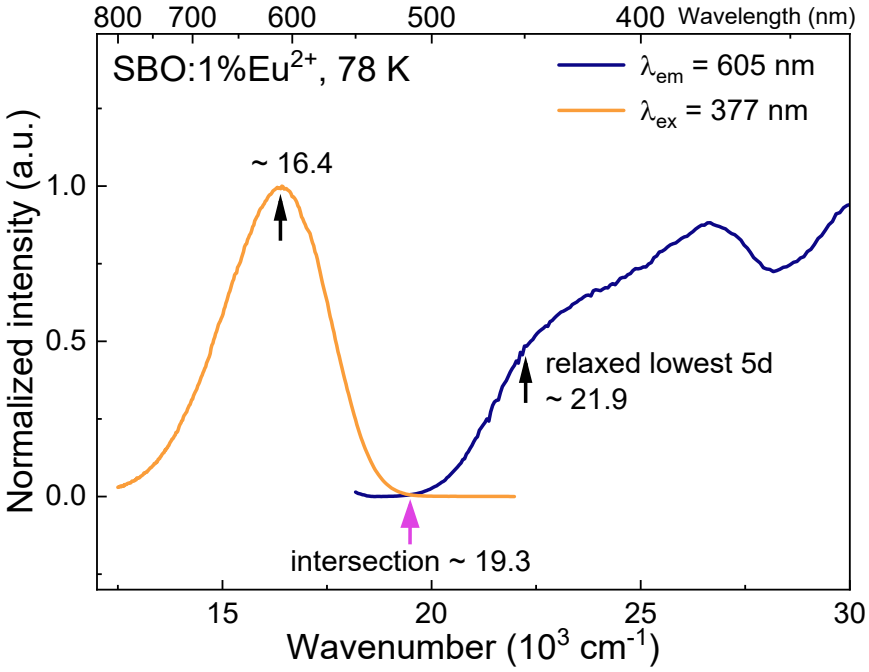

Fig. S8. Highest-height normalized excitation (λ_{em} = 605 nm) and emission (λ_{ex} = 377 nm) spectra of SBO:1%Eu^{2+} at 78 K.

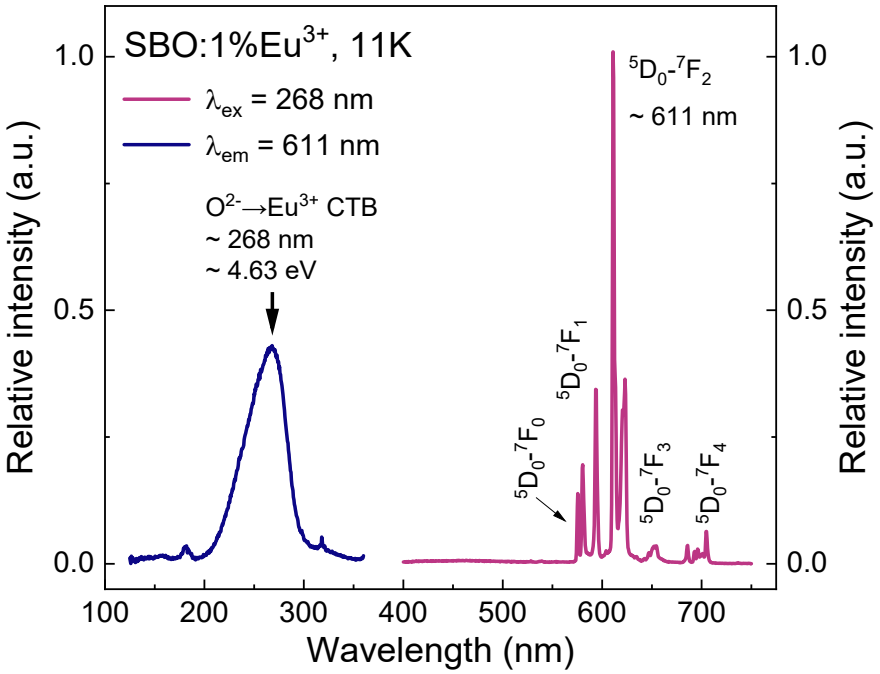

Fig. S9. VUV-UV excitation (λ_{em} = 611 nm) and emission (λ_{ex} = 268 nm) spectra of SBO:1%Eu^{3+} at 11 K.

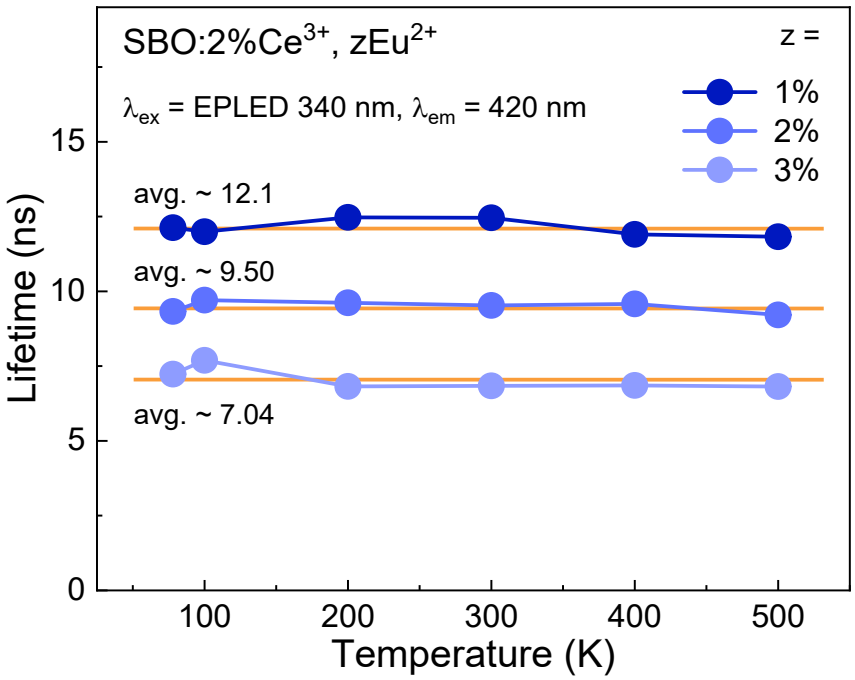

Fig. S10. Extracted temperature-dependent (78-500 K) Ce^{3+} emission lifetime values of SBO:2%Ce^{3+}, zEu^{2+} (z = 1%-3%).

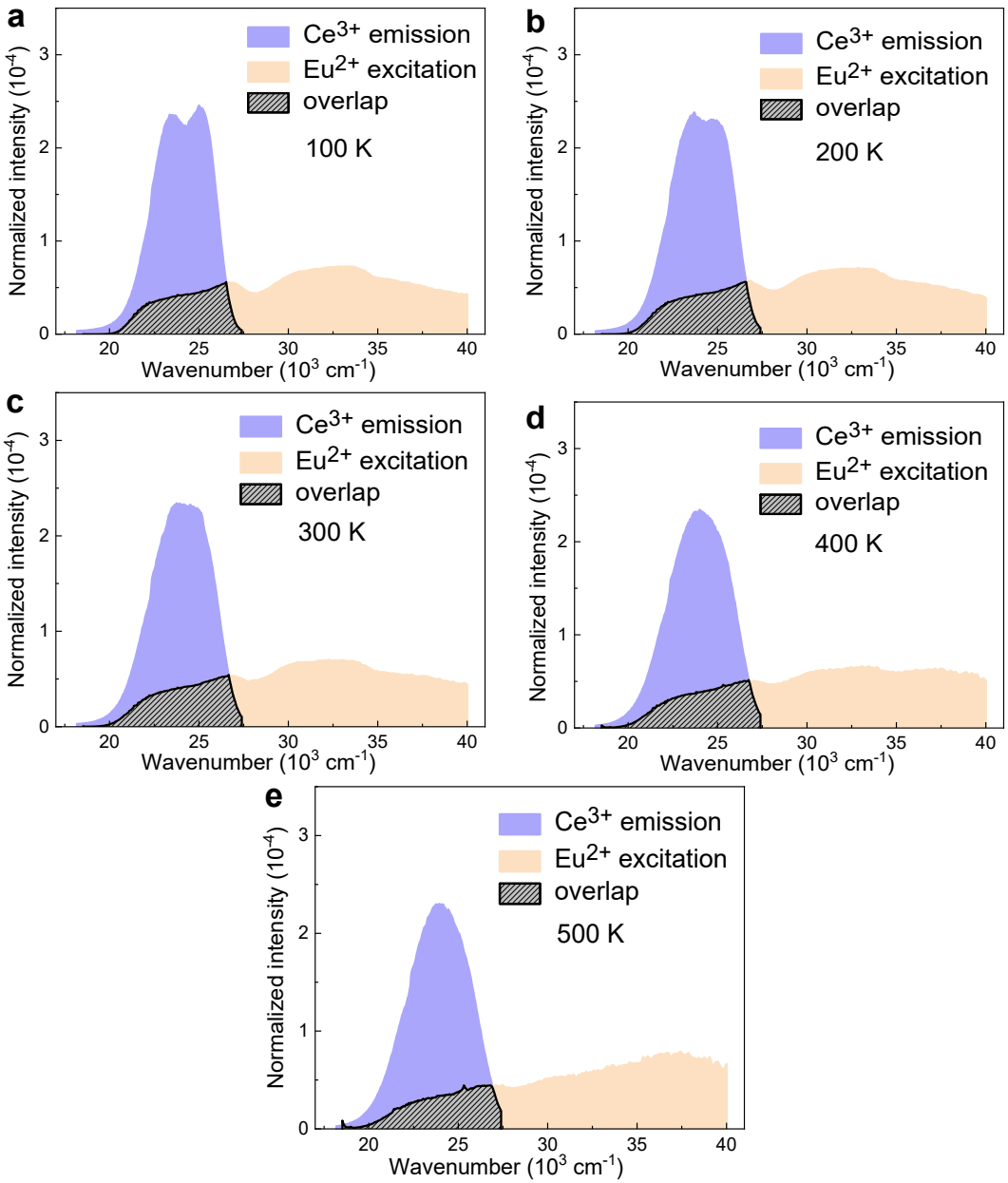

Fig. S11. Spectral-overlapping integrated area between Ce^{3+} emission (SBO:1%Ce^{3+}, λ_{ex} = 340 nm) and Eu^{2+} excitation spectra (SBO:1%Eu^{2+}, λ_{em} = 605 nm) at elevated temperature (100-500 K).

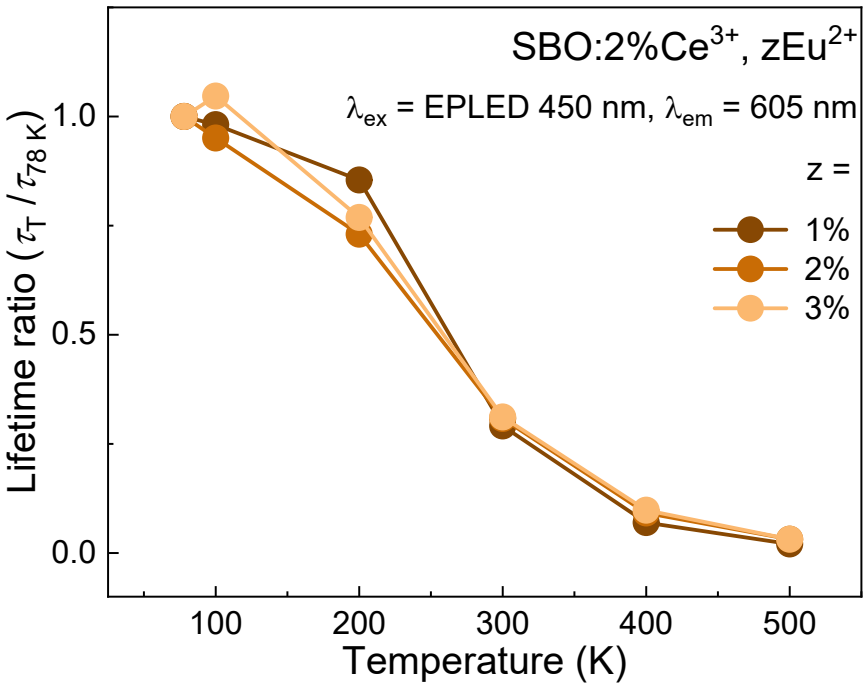

Fig. S12. Temperature-dependent (78-500 K) Eu^{2+} emission lifetime ratios (τ_T / $\tau_{78\ K}$) of SBO:2%Ce^{3+}, zEu^{2+} (z = 1%-3%).

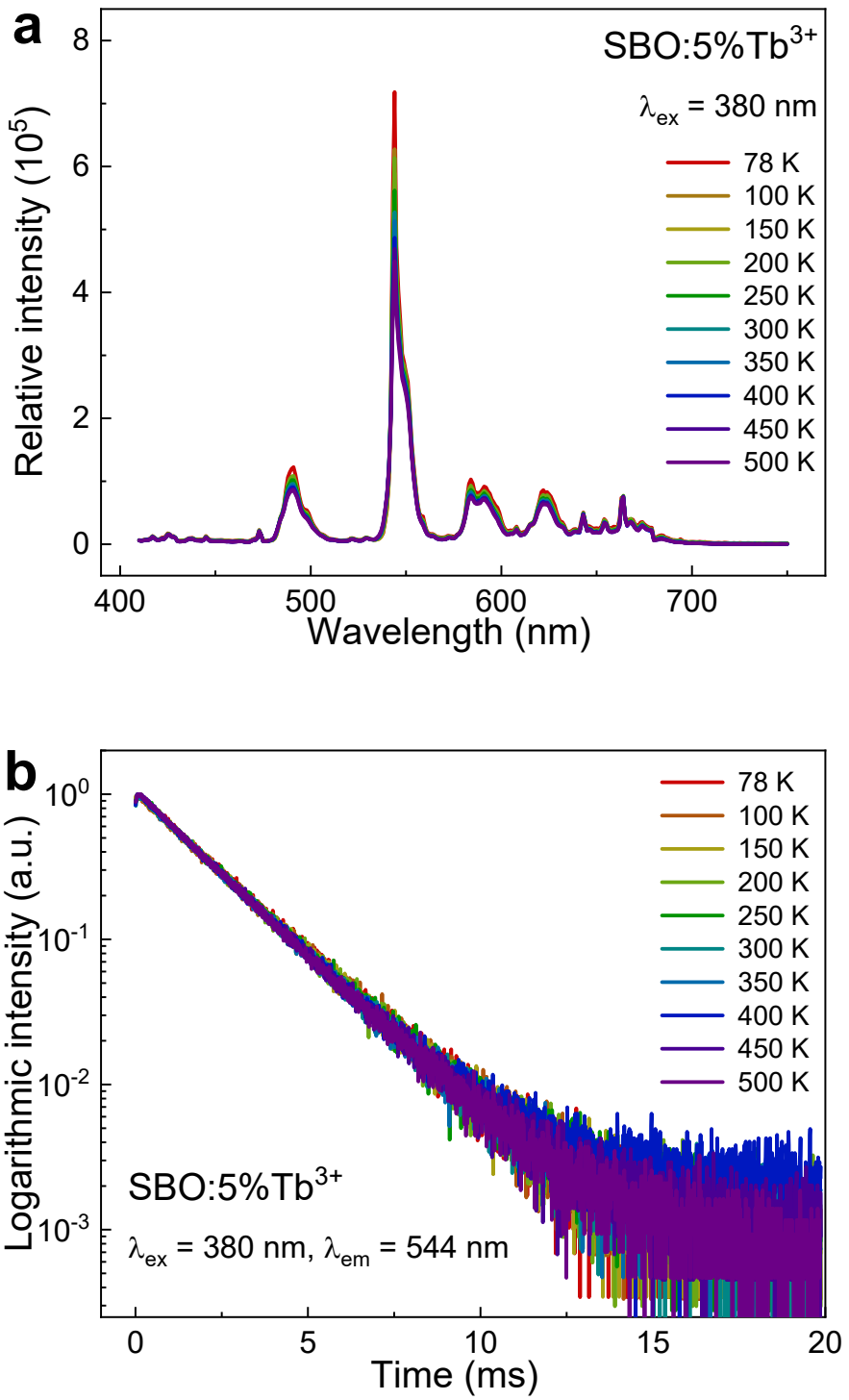

Fig. S13. Temperature-dependent (78-500 K) Tb^{3+} emission (a, λ_{ex} = 380 nm) spectra and luminescence decay curves (b, λ_{ex} = 380 nm, λ_{em} = 544 nm) of SBO:5%Tb^{3+}.

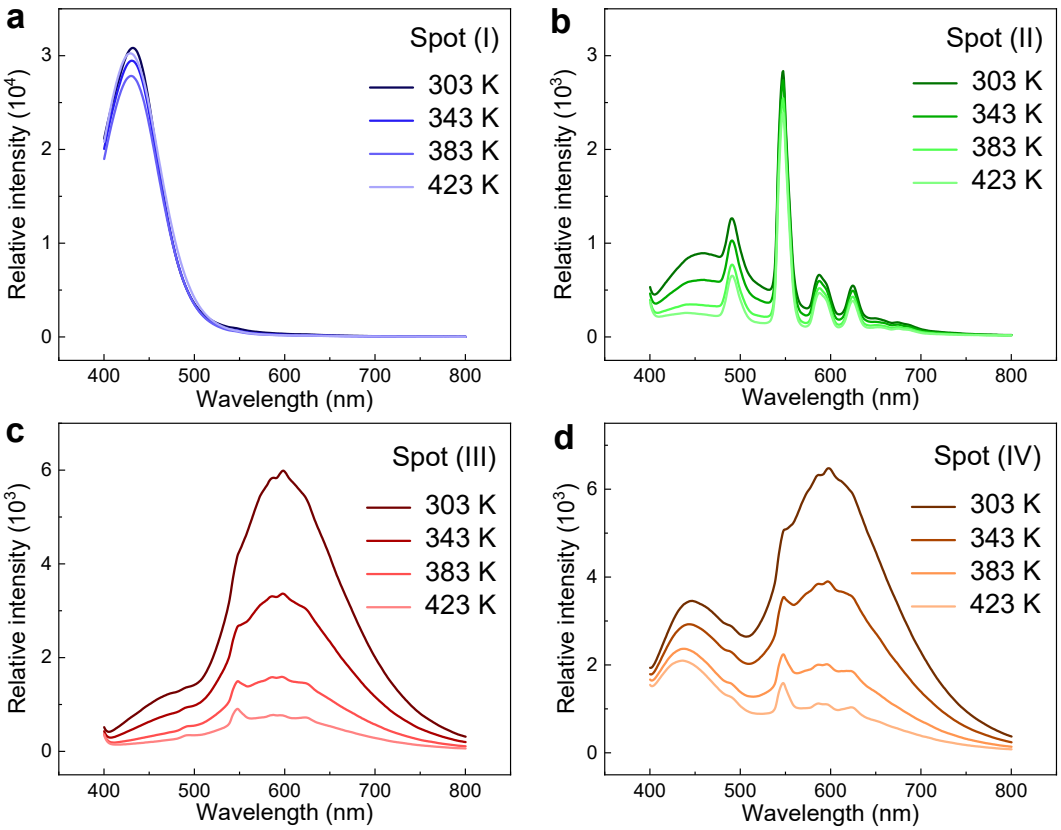

Fig. S14. Temperature-dependent (303-423 K) emission spectra of spots (I-IV) in colour-mode security tag collected by optical fibre spectrometer under 365 nm lamp irradiation.

Due to the sensor size of optical fibre spectrometer, the collected emission spectrum of certain spot may be slightly influenced by emissions from other spots or resin cover. For examples, the broad band signal peaking at ~ 450 nm in spot (II) emission is attributed by the organic fluorescence of resin cover, which shows poor thermal stability; the sharp-line emissions at ~ 544 nm in emissions of spots (III) and (IV) are aligned to the Tb^{3+} luminescence in spot (II). However, these disturbances would not significantly affect the image evolution performance of colour-mode security tag as shown in Fig. 5c.

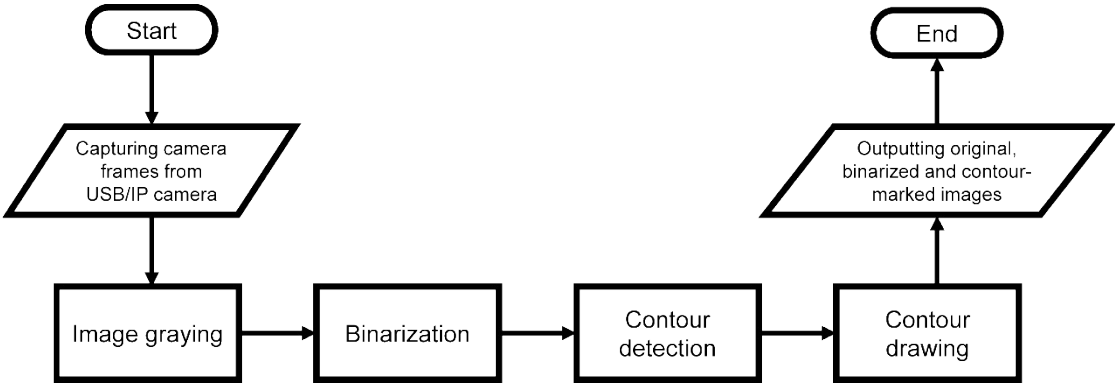

Fig. S15. Flow chart of real-time identification process on intensity-mode security tag with computer vision technique.

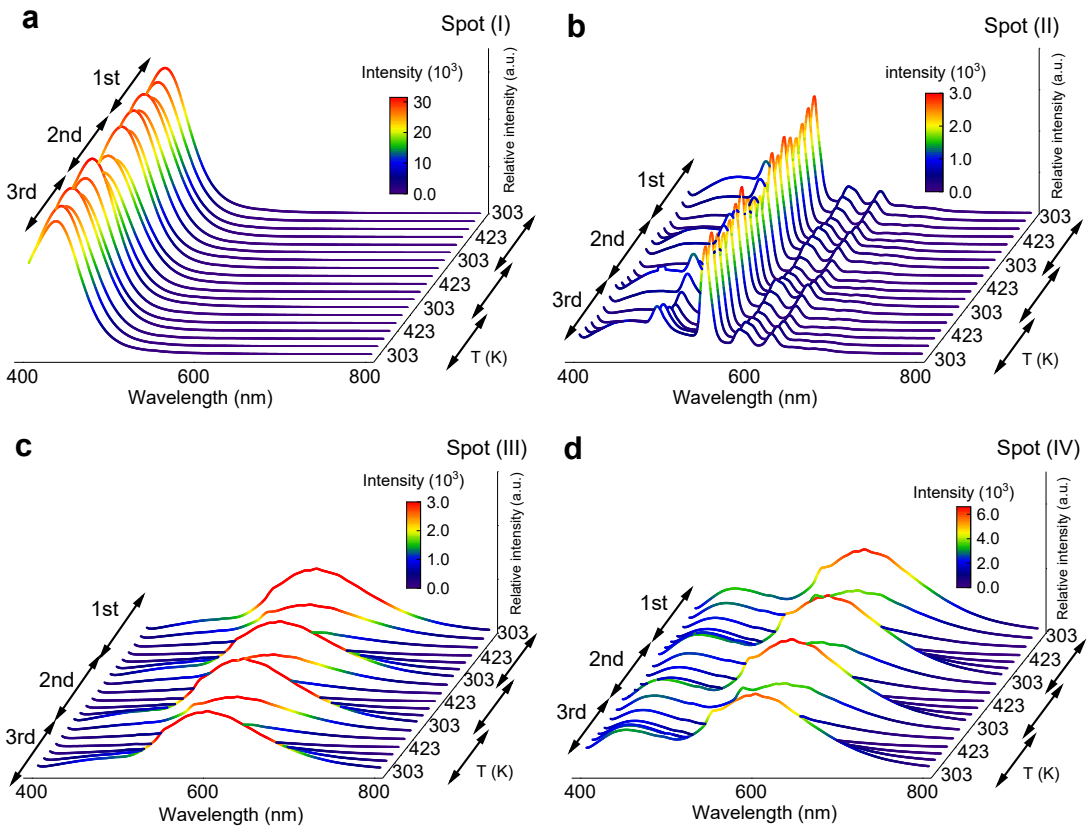

Fig. S16. Temperature-dependent (303-423 K) emission spectra of spots (I-IV) in colour-mode security tag in three temperature cycles.

References

(1) A. A. Coelho, Coelho Software, Version 4, *Topas Academic*, Brisbane, Australia, 2007.

(2) C. Hu, X. Wang, Z. Qi and C. Li, *Infrared Phys. Technol.*, 2020, **105**, 103200.

(3) A. B. Kuzmenko, *Rev. Sci. Instrum.*, 2005, **76**, 083108.

(4) Y. Tao, Y. Huang, Z. Gao, H. Zhang, A. Zhou, Y. Tan, D. Li and S. Sun, *J. Synchrotron Radiat.*, 2009, **16**, 857-863.

(5) G. Kresse and J. Furthmüller, *Phys. Rev. B*, 1996, **54**, 11169-11186.

(6) G. Kresse and D. Joubert, *Phys. Rev. B*, 1999, **59**, 1758-1775.

(7) P. E. Blöchl, *Phys. Rev. B*, 1994, **50**, 17953-17979.

(8) J. P. Perdew, K. Burke and M. Ernzerhof, *Phys. Rev. Lett.*, 1996, **77**, 3865-3868.

(9) J. P. Perdew, M. Ernzerhof and K. Burke, *J. Chem. Phys.*, 1996, **105**, 9982-9985.

(10) E. Y. Borovikova, E. A. Dobretsova, K. N. Boldyrev, V. S. Kurazhkovskaya, V. V. Maltsev and N. I. Leonyuk, *Vib. Spectrosc.*, 2013, **68**, 82-90.

(11) P. Dorenbos, *ECS J. Solid State Sci. Technol.*, 2013, **2**, R3001-R3011.

(12) P. Dorenbos, *J. Lumin.*, 2020, **222**, 117164.

(13) M. Inokuti and F. Hirayama, *J. Chem. Phys.*, 1965, **43**, 1978-1989.

(14) P. Dorenbos, *J. Lumin.*, 2019, **214**, 116356.

(15) P. Dorenbos, *Opt. Mater.*, 2017, **69**, 8-22.

(16) P. Dorenbos, *J. Lumin.*, 2013, **135**, 93-104.

(17) F. Su, W. Zhou, Y. Yang, Y. Ou, Z. Qi, C.-K. Duan, M. G. Brik, P. Dorenbos and H. Liang, *Dalton Trans.*, 2021, **50**, 10050-10058.